Microstructure and mechanical properties of a high Nb-TiAl alloy fabricated by electron beam melting

Kan, W., Chen, B., Jin, C., Peng, H. & Lin, J.

Microstructure and mechanical properties of a high Nb-TiAl alloy fabricated by electron beam melting

W. Kan [a], B. Chen [b], C. Jin [c], H. Peng [d,e,*], J. Lin [a,**]

[a] State Key Laboratory for Advanced Metals and Materials, University of Science and Technology Beijing, Beijing 100083, China
[b] The Institute for Future Transport and Cities, Faculty of Engineering, Environment and Computing, Coventry University, Coventry CV1 5FB, UK
[c] Department of Mechanical Engineering, Binghamton University, Binghamton, NY 13902, USA
[d] Key Laboratory of High-Temperature Structural Materials & Coatings Technology, Ministry of Industry and Information Technology, Beihang University, Beijing 100191, China
[e] School of Materials Science and Engineering, Beihang University, Beijing 100191, China

HIGHLIGHTS

- A fundamental principle is proposed to control the microstructure of Nb-TiAl alloy in EBM with competitive tensile properties.

GRAPHICAL ABSTRACT
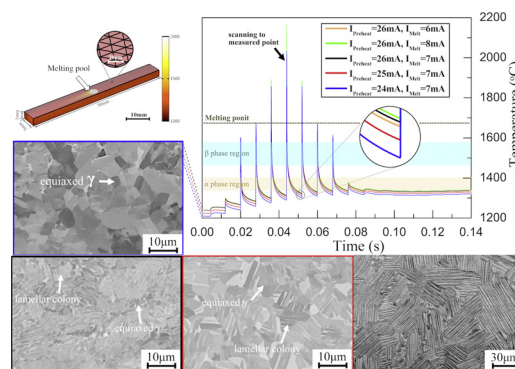
ARTICLE INFO

ABSTRACT

Electron beam melting (EBM) has been applied to fabricate a high Nb-TiAl alloy with a fully dense microstructure and good tensile properties at both room and high temperatures. The effects of preheating and melting parameters on melting, solidification, phase transformation and resulting microstructure formation in as-EBM high Nb-TiAl alloy were investigated by performing a design-of-experiments. Results show that the limited EBM processing window can be broadened to produce different characteristic microstructures ranging from nearly fully lamellar γ/α_2 to equiaxed γ grains. Such a broadened processing window has been achieved by using stronger preheating beam current. A numerical simulation was performed to understand temperature evolution at a fixed point of interest where electron beam passed several times with a certain line offset within one build layer. Both the preheating and melting stages were considered in the model. Modelling results show that a higher preheating beam current resulted in a longer hold time within the temperature range between 1300 and 1380 °C (i.e. single α-phase region). This helped to produce fine lamellar microstructure in the high Nb-TiAl alloy. Fundamental principles are thus proposed in terms of controlling microstructure formation and fabricating fully dense high Nb-TiAl alloy in as-EBM condition.

© 2018 Elsevier Ltd. All rights reserved.

 * Correspondence to: H. Peng, Key Laboratory of High-Temperature Structural Materials & Coatings Technology, Ministry of Industry and Information Technology, Beihang University, Beijing 100191, China.
 ** Corresponding author.
    E-mail addresses: penghui@buaa.edu.cn (H. Peng), linjunpin@ustb.edu.cn (J. Lin).

1. Introduction

Advanced γ-TiAl intermetallic alloys have the potential to replace the heavier Ni-base superalloys for high-temperature applications such as low-pressure turbine blades because of their low density of about 4 g/cm³, high melting point, good creep and oxidation performance up to 750 °C, as well as burn resistance [1]. High Nb-TiAl alloys have been metallurgically designed and developed to further enhance their oxidation resistance and creep properties [2]. However, fabrication of intricate Ti-(42-48)Al-(6-10)Nb (in at.%) parts and components by conventional means including forging, rolling and welding remains as a challenge [3,4]. This is due to γ-TiAl intrinsic room-temperature brittleness and inadequate hot workability [5]. Fabricating γ-TiAl alloy by precision casting was also reported to be difficult, due to its high activity and bad fluidity of the fusant [6].

Electron beam melting (EBM) and selective laser melting (SLM) are the two most commonly used additive manufacturing processes. Compared to SLM, EBM operates with a much higher build temperature and hence a lower residual stress is normally generated in the EBM build [7,8]. By operating above the ductile-to-brittle transition temperature (DBTT, ~800 °C for TiAl alloys [9]), EBM can be used to fabricate Ti-48Al-2Cr-2Nb [2]. Cormier et al. [10] and Murr et al. [11] demonstrated the feasibility of EBM fabricating bulk Ti-47Al-2Cr-2Nb alloy. Biamino et al. reported that good tensile properties in an EBM Ti-48Al-2Cr-2Nb [12] and a high Nb-TiAl alloy [13] both in post-processed conditions (i.e. after hot-isostatic-pressing, HIP, and heat treatment) can be obtained, however no comment was given to the as-EBM condition.

Schwerdtfeger and Korner [14] investigated systematically EBM processing window for Ti-48Al-2Cr-2Nb alloy. A reduced Al loss of about 0.5 at.% can be achieved by using a lower beam current and adjusting other parameters accordingly that included layer thickness, scanning speed and line offset [14]. This is very important to γ-TiAl alloy as the Al loss would strongly affect the microstructure formation and resulting mechanical performance. It was also commented in [14,15] that a higher build temperature by using stronger preheating parameters (i.e. longer duration and higher beam current) led to an improved process stability by avoiding the formation of smoke. A recent work by Todai et al. [16] revealed that tensile properties of as-EBM Ti-48Al-2Cr-2Nb were higher than that prepared by casting, owing to the development of much finer microstructures. Despite success in EBM fabricating Ti-48Al-2Cr-2Nb, it is still unclear whether EBM can be used to fabricate high Nb-TiAl alloy whose high-temperature mechanical properties are deemed to be more superior than Ti-48Al-2Cr-2Nb [17,18]. It is worth noting that a severer room-temperature brittleness occurs in γ-TiAl alloy with increasing Nb content [17].

To date, the work by Tang et al. [19] is the only EBM study on high Nb-TiAl alloy. A self-made EBM machine was used to fabricate Ti-45Al-7Nb-0.3W alloy. It was concluded that as-EBM samples were far from pore-free and subsequent HIP would be required to remove the pores. The room-temperature compression properties in the as-EBM samples were found to be as good as those fabricated by conventional methods [19,20]. Tensile properties of the EBM samples were not reported in the work [19]. There are three research gaps related to high Nb-TiAl that requires attention: (i) the difficulty to retain the fine microstructure by performing a post-EBM HIP treatment; (ii) the difficulty to obtain optimised lamellar microstructure by performing a post-EBM heat treatment; and (iii) the EBM processing window is relatively narrow to obtain desired microstructures and properties. The former two relates to the fact that excessive growth of lamellar colony grains occurs in single α-phase region (between 1300 and 1380 °C) [21]. The third is due to a classic dilemma in EBM fabrication between creating a fully dense microstructure that would require a greater energy input [14] and avoiding light element evaporation that favours a lower energy input [14]. A greater energy input may cause serious Al loss due to the high saturated vapour pressure of Al compared with Ti and Nb [14,22]. Hence, the present work deals with the prospects for EBM processing

of a high Nb-TiAl alloy, Ti-45Al-8Nb, with a particular focus to reveal the fundamental principles to obtain a fully dense sample with a fully lamellar microstructure, which does not depend on the post-EBM HIP and/or heat treatment.

EBM is a considerably complicated process that involves heat conduction, melting, boiling, evaporation, and even the phase explosion [23]. Therefore, experiments alone are far from enough to clarify the thermal history and the interaction between the electron beam and the material. Previous work [23,24] demonstrated that numerical simulation is a powerful tool to help discerning the temperature evolution during EBM process so that the microstructure formation can be correlated with the temperature profile. To this end, a thermal numerical model that provides the temperature field is employed in the present work to aid interpreting the solidification and phase transformation that occurs during the EBM process.

2. Experimental

2.1. Ti-45Al-8Nb powders

Rapidly solidified pre-alloyed powders with a nominal composition of Ti–45Al–8Nb (fabricated by Sailong Metal) were utilised for the EBM fabrication. These powders were produced by plasma rotating electrode process (PREP). The ingot was molten twice to achieve chemical compositional homogeneity prior to PREP. Chemical composition of the powders was analysed by using inductively coupled plasma atomic emission spectroscopy (NCS Testing Technology Co., Ltd.). X-ray diffraction (XRD) were carried out to identify the phase constitution of PREP powders using a Bruker D8 Advance with Cu Kα diffraction (40 kV, 40 mA). The flowability of PREP powders was examined by the Hall flow test according to ASTM B213 standard, and the powder flowability met the requirement for the EBM process.

To visualise powder surface structure, size distribution and microstructure, a Carl Zeiss Supra 40 VP field emission scanning electron microscope (SEM) was used. For this purpose, the Ti-45Al-8Nb powders were either attached to a stub by carbon tape or embedded into bakelite mounting resin. The particle size distribution was measured and analysed using an image analysis software (ImageJ). Imported SEM micrographs containing over 200 powder particles were processed to a binary image threshold to identify individual particles. The number of particles within a 20 μm diameter interval was then counted from these SEM micrographs and finally calculated to obtain the size distribution.

2.2. EBM processing

An Arcam A2XX machine with Control Software 3.2 was used in manual mode for the EBM fabrication of high Nb-TiAl samples. A 70 μm thick layer of pre-alloyed PREP Ti-45Al-8Nb powders was raked onto the build starting plate, followed by electron beam scanning over the powder layer in a pre-defined pattern to achieve powder consolidation to the final dense metal sample. There are two distinct stages for the EBM process: preheating and melting. In terms of the preheating, a strongly defocused beam is used to ensure mechanical stability and electrical conductivity to prevent powder charge problem. In contrast, a focused beam scanning at a relatively low speed is used for melting the powders in the melting stage. For suppressing the powder charge more effectively, the preheating stage is further divided into two steps. A lower beam energy is often used in preheat I to achieve semi-sintering of powders, thereafter a higher beam energy is used in preheat II to obtain a higher preheating temperature. The higher preheating beam energy can be achieved by either multiple scans or higher beam current. In the present work, average preheating beam current[1] in

---

[1] Average beam current is a critical parameter for heat balance calculation in the EBM control® software.

preheat II was varied from 24 to 26 mA to produce different preheating conditions, Table 1. According to [25], area energy E_A is a function of accelerating voltage U, beam current I, scanning speed v and line offset L_{off}. E_A can be expressed as:

$$E_A = \frac{UI}{vL_{off}} \tag{1}$$

U was fixed to 60 kV and L_{off} was fixed to 100 μm in this work. A scanning speed of 20,000 mm/s was used in preheat II and this resulted in an equivalent area energy ranging from 0.72 W/(mm^2/s) to 0.78 W/(mm^2/s) for the corresponding beam current of 24 mA and 26 mA, Table 1. In addition, melting beam current and scanning speed, were varied from 6 to 7 mA and 2100 to 2700 mm/s, respectively, to produce different melting conditions, Table 2. Cubic samples of 30 × 30 × 30 mm^3 were produced in total 3 groups: group A in Table 1 and groups B and C in Table 2. The preheating parameters were changed for samples A1, A2 and A3 but with the same melting parameters, whereas the melting parameters were changed for groups B and C but with the same preheating parameters ($I_{preheat}$ = 25 mA and E_A = 0.75 W/(mm^2/s)). This set of design-of-experiments allowed us to assess the effects of both preheating and melting parameters on the resulting microstructure formation in EBM fabrication of Ti-45Al-8Nb alloy.

The samples were fabricated by a line order EBM scanning strategy where the electron beam scans in a snake-like way. The hatch melting direction was changed by 90° after each build layer. A detailed description about EBM hatch melting together with a schematic illustration can be found in [26]. No supports were applied for the EBM sample fabrication.

Fig. 1(a) illustrates a typical batch of the EBM build, where four individual samples were fabricated with a preheating area of 100 mm × 100 mm from the top of the starting plate with a diameter of 155 mm. It was found that at least 24 mA in preheat II was required to maintain the build temperature[2] of above 1000 °C, so that a stable fabrication process can be achieved. Although the preheating beam current difference is small for preheat II as listed in Table 1, the temperature effect should not be ignored. We will discuss this in detail together with the modelling results. Furthermore, because of the narrow EBM processing window for TiAl alloys [14], the selected scanning speed range from 2100 to 2700 mm/s is relatively small, Table 2.

The build temperature as a function of the elapsed time is shown in Fig. 1(b) to provide indicative information in terms of the thermal history of one batch of the EBM build. There are three stages as indicated in Fig. 1(b). After preheating the starting plate to the temperature of ~1180 °C, the EBM fabrication process started and the total build took about 10 h per batch. The initial temperature changes within the first 3 mm build, as shown by stage I in Fig. 1(b), were associated with the gradual starting plate coverage by the powder layers, i.e. the initial large heat dissipation area of 155 mm in diameter to a subsequent smaller square area of 100 mm × 100 mm. This accounted for the measured temperature decreased first, followed by a rise, see stage I in Fig. 1 (b). The temperature fluctuation as shown by stage II in Fig. 1(b), was caused by the fine parameter adjustment with the aim to achieve a later more stable EBM process, stage III in Fig. 1(b). The processing parameters were not changed in stage III and the measured build temperature stabilised at above 1000 °C. This corresponded to the sample build heights from 8 mm to 30 mm. The whole EBM fabrication took 20 h that included 10 h for the actual build and another 10 h for the slow cooling to room temperature.

Table 1
Preheating and Melting parameters used to EBM fabricate Ti-45Al-8Nb samples A1, A2 and A3 where preheating beam current was changed for each sample.

Sample ID	Preheat II process		Melting process		
	Average beam current, mA	Area energy, W/(mm^2/s)	Beam current, mA	Scanning speed, mm/s	Area energy, W/(mm^2/s)
A1	26	0.78	7	2000	2.10
A2	25	0.75			
A3	24	0.72			

2.3. Microstructural characterisation and mechanical testing

As-EBM samples were cut by wire electrical discharge machining (WEDM) to obtain vertical and horizontal cross-sections; the region of interest for microstructural analysis is shown in Fig. 1(c). All the microstructural characterisation was performed at the centre position of the as-EBM samples, i.e. 15 mm distance to the vertical sectional plane. Samples for metallographic examinations were ground down to 2500 grit SiC paper, polished down to 1 μm diamond paste and finally electrolytic polished using a chemical solution (5% perchloric acid + 30% butanol + 65% methanol).

A back scattered electron (BSE) imaging mode (Carl Zeiss Supra 40 VP SEM) was used to reveal the microstructural features. The percentage of lamellar colony grains for each EBM processing parameter sets, group A in Table 1 and group B and C in Table 2, was quantitatively analysed based on at least 10 different SEM micrographs at a similar build height of 15 mm as indicated in Fig. 1(c). Each SEM micrograph typically contained 20 to 50 colony grains. The chemical compositional homogeneity of as-EBM samples was also examined with the help of BSE imaging mode as Schwerdtfeger and Korner [14] reported that EBM TiAl alloys are susceptible to the light element evaporation, i.e. Al loss. The vertical cross-section of as-EBM samples was examined. The phase identification was performed by a Bruker D8 Advance with Cu Kα radiation at 40 kV and 40 mA. Chemical composition analysis for the as-EBM Ti-45Al-8Nb sample was performed by using inductively coupled plasma atomic emission spectroscopy. The relative density of samples was measured using Archimedes drainage method [27,28]. A Tecnai G2 F30 field-emission transmission electron microscope (TEM) operating at 300 kV was used to reveal the α_2/γ fine microstructural features within lamellar colony grains. The TEM thin foils were prepared by first grinding down to ~100 μm thick, punched to a 3 mm disc, finally twin-jet electro-polishing to create electron transparency.

Uniaxial tensile tests were performed on an electronic universal testing machines (DDL 50, Changchun Research Institute for Mechanical Science Co., Ltd.) at room temperature, 800 and 900 °C with a strain rate of 5×10^{-4} s^{-1}. The tensile loading direction applied to the specimen was parallel to the horizontal direction, i.e. perpendicular to the EBM build direction. These miniaturised tensile test specimens with a

Table 2
Summary of EBM parameters selected for evaluating the effect of beam current and scanning speed during melting process.

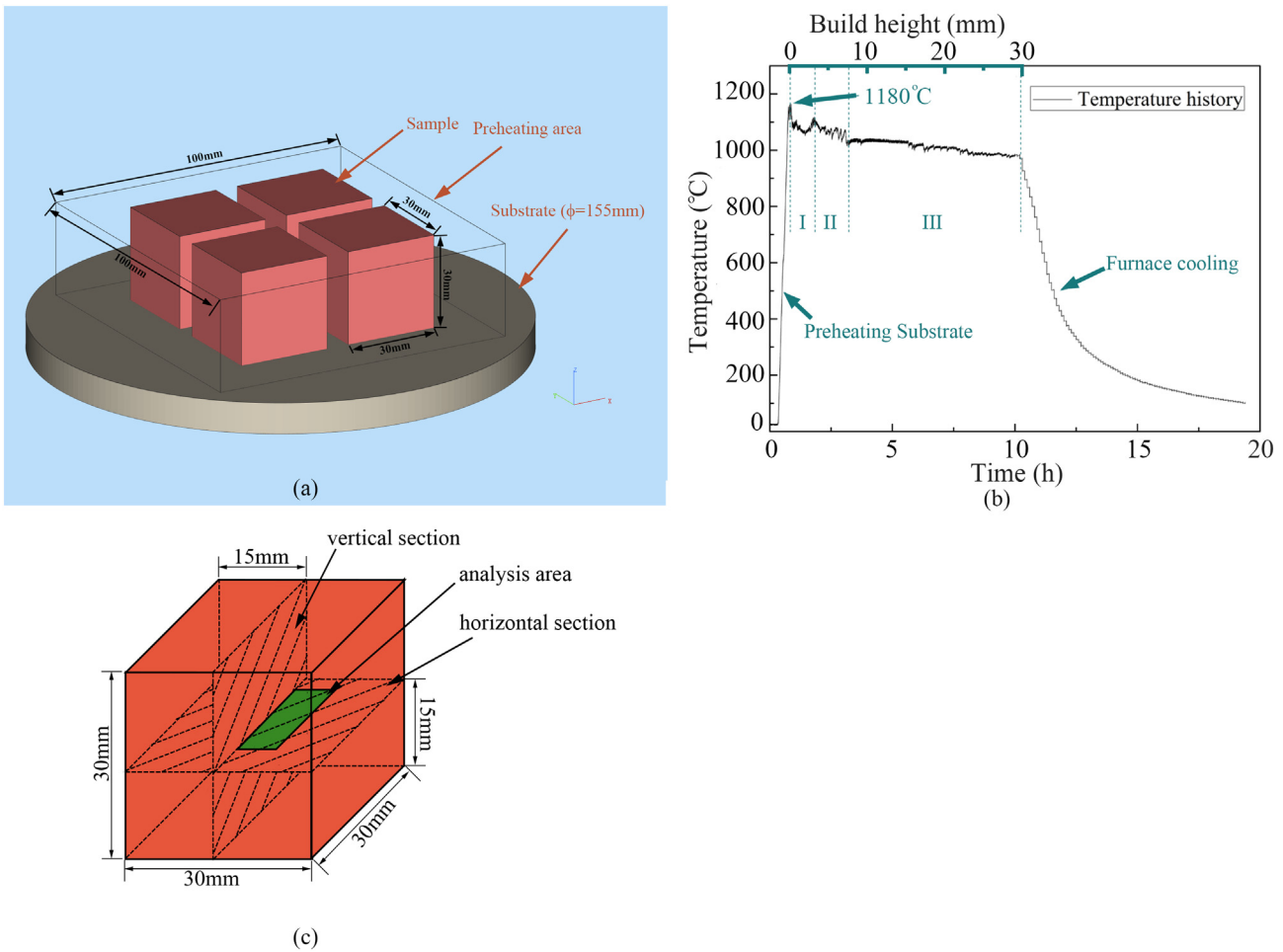| Sample ID	Melting process				Density, g/cm^3	Al loss, at.%
	Beam current, mA	Scanning speed, mm/s	Energy input, W	Area energy, W/(mm^2/s)		
B1	7	2100	420	2.00	4.25	1.3
B2		2300		1.83	4.24	0.9
B3		2500		1.68	4.20	0.5
B4		2700		1.56	4.18	1.1
C1	6	2300	360	1.57	4.17	0.7
C2	7		420	1.83	4.22	0.8
C3	8		480	2.09	4.25	1.7

Fig. 1. (a) A schematic illustration of the EBM sample build; (b) The build temperature measured by a thermocouple attached to the bottom of the build starting plate; (c) A schematic diagram showing the WEDM sample cuts for the metallographic examination.

gauge length of 10 mm and a cross-sectional area of 3 mm × 1 mm were extracted by WEDM at the build height position close to 15 mm. The gauge length of the tensile specimen was 10 mm, and the cross-sectional area was 3 mm × 1 mm. For comparison, cast-TiAl (Ti-45Al-8Nb) samples in heat treated condition were also tensile tested.

3. Numerical modelling

3.1. Overall description of model set-up

Fig. 2(a) and (b) depicts schematically the finite element modelling set-up for preheating and melting stages, respectively. The temperature fields during electron beam moving for both stages were obtained by using a commercial finite element software Comsol (Version 5.2). Considering the computational cost and calculation efficiency, numerical simulation of the temperature field was not a continuous process. In general, the simulation can be divided into two parts: preheating and melting. In terms of the preheating, the model was built with a dimension of $30 \times 30 \times 15 \text{ mm}^3$, as shown in Fig. 2(a). This geometric dimension and the top surface position corresponded to that examined by microstructural observation. In terms of the melting, the dimension of the model was $30 \times 3 \times 1 \text{ mm}^3$ as shown in Fig. 2(b). The reduced geometric dimension helped to save unnecessary computational cost as the local temperature was affected mainly by the neighbouring scanning
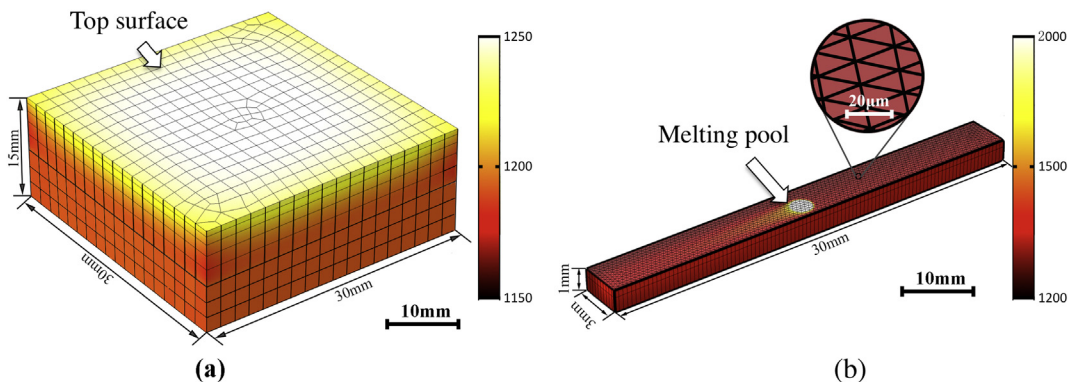

Fig. 2. The numerical model set-up for simulating (a) preheating stage and (b) melting stage.

lines during the melting process. A relatively coarse mesh was adopted for the preheating simulation, Fig. 2(a), while an extremely refined mesh with 18,720 elements and 9736 nodes was used for the melting simulation, Fig. 2(b). The preheating and melting process simulation were connected by using the parameter T_{local} in the model. In detail, T_{local} represented not only the average temperature of the top surface at the finish of preheating, Fig. 2(a), but also the initial temperature for the melting process, Fig. 2(b). Thereafter, the temperature profile at a fixed point of interest at the central part of the top surface was extracted from the melting simulation.

There were only three $I_{preheat}$ conditions considered in the design-of-experiments, $I_{preheat}$ = 24, 25 and 26 mA, Table 1. For all three preheating conditions, T_{local} was calculated with the iteration time duration of 20 s, that is similar to the actual time spent in the EBM process. In the melting process simulation, the electron beam moved in the same way to that applied in the experiment, i.e. L_{off} = 100 μm and additional electron beam parameters used for the simulation are given in Table 3. The variation of the reciprocating period caused by the change of scanning speed in the melting process was not considered in the present model. This is because an increased scanning speed would result in a reduction in beam return time and hence increasing the thermal impact of adjacent scanning lines. But an increased scanning speed also leads to a reduced heat input per unit area, E_A. To this end, only the different melting beam currents ranging from I_{melt} = 6 to 8 mA were considered in the model and their influence on the resulting microstructure formation were assessed.

The temperature field during the EBM process is governed by melting, solidification, conduction, radiation, evaporation, etc. [23,29,30]. The main focus of the model was on the temperature range between 1000 and 1400 °C where lamellar colony and/or equiaxed γ grains formed in high Nb-TiAl alloy. The fluid dynamics was not considered in the present model in order to simplify the calculation. As described in [31], this simplification should not affect us to assess the temperature field in the range of interest, i.e. between 1000 and 1400 °C.

Fig. 3 shows a typical temperature profile obtained by the numerical simulation for the melting process. In this case, $I_{preheat}$ = 25 mA and I_{melt} = 7 mA were used in the model. A video illustration of the simulation can be found in the supplementary material. T_{local} as indicated in Fig. 3 represents the temperature at the end of the preheating stage, and the Numbers 1–12 as indicated in Fig. 3 are each individual electron beam scanning passes. As mentioned above, the temperature profile at a fixed point (Number 6 in Fig. 3) at the central part of the top surface was monitored in our model simulation. As shown in Fig. 3, when the focused electron beam was scanned close to the measured point of interest, the temperature rapidly raised above the melting point. Thereafter, rapid solidification occurred, followed by a fast cooling rate of about 3×10^6 °C/s from 1896 to 1596 °C and annealing in the single α-phase region for a relatively long time. After the focused electron beam moved to the next adjacent scanning passes, the temperature filed at the measured point still oscillated strongly, for example Numbers 8–10 in Fig. 3.

Table 3
Summary of temperature-dependent thermophysical parameters and EBM processing simulation parameters.

Temperature, T (°C)	1000	1200	1400	1600	1800
Thermal conductivity, κ (W/m °C)	7.76	7.83	22.91	39.12	42.54
Specific heat capacity, c (J/kg °C)	709	729	749	769	789
Density, ρ (kg/m³)	3250	3208	3096	2990	2920
Enthalpy, H (kJ/kg)	−406	−198	21	685	1021
Convective heat-transfer coefficient, h_c	80 W/(m² K)				
The Stefan-Boltzmann constant, σ_e	5.6710^{-8} W/(m² K⁴)				
Radius of the Gaussian beam, ω	100 μm				
Absorptivity, B	0.7				
Radiation emissivity, ε	0.36				
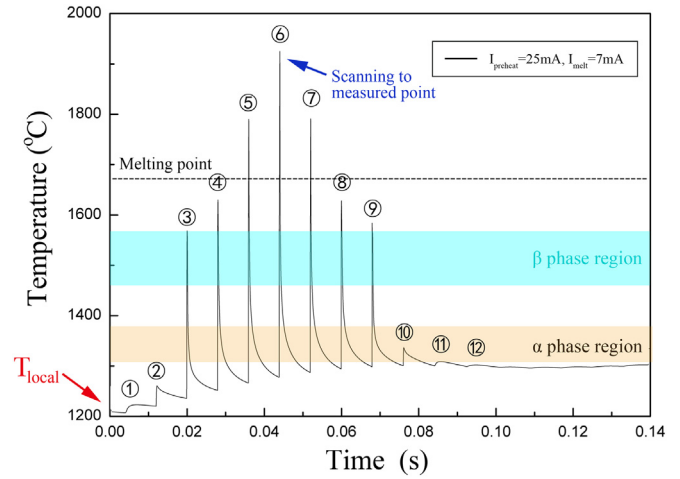
Fig. 3. A typical temperature profile observed at a fixed point of interest for the melting process. In total 12 melting scan passes were simulated.

3.2. Heat source, heat flux and thermophysical parameters

For the thermal field numerical simulation, apart from the consideration of the thermal conduction, the heat losses associated with convection and radiation were also taken into account. The spatial and temporal temperature field distribution obeys the differential equation of 3D heat conduction, according to [23]:

$$\rho c \frac{\partial T}{\partial t} = \frac{\partial}{\partial x}\left(\kappa \frac{\partial T}{\partial x}\right) + \frac{\partial}{\partial y}\left(\kappa \frac{\partial T}{\partial y}\right) + \frac{\partial}{\partial z}\left(\kappa \frac{\partial T}{\partial z}\right) + Q \tag{2}$$

where ρ is material density, c is the specific heat capacity and κ is the thermal conductivity of solid Ti-45Al-8Nb. T is the temperature for the region of interest, t is the interaction time between the electron beam and the system, and Q is the heat generated per volume within the system. The boundary condition for heat transfer under electron beam irradiation can be expressed as [23]:

$$-\kappa \frac{\partial T}{\partial z} = q_{beam} - q_{conv} - q_{radi} (x, y, z) \in S \tag{3}$$

where S is the top surface area of 30×30 mm² as indicated in Fig. 2(a). The heat conduction, convection and radiation occurred from this surface. n is the normal vector of top surface S, and q_{beam} is the heat input generated by a Gaussian heat source, that will be described later in Eq. (6). q_{conv} is the heat convection and q_{radi} is the heat radiation and can be expressed by [23]:

$$q_{conv} = h_c(T - T_\infty) \tag{4}$$

$$q_{radi} = \varepsilon \sigma_e \left(T^4 - T_\infty^4\right) \tag{5}$$

where h_c is the convective heat-transfer coefficient, σ_e is the Stefan-Boltzmann constant, and ε is the radiation emissivity. Their values are given in Table 3. T_∞ is the room temperature and is taken as 300 K.

The moving electron beam acting as the energy input source was modelled with a Gaussian distribution of beam intensity, which can be expressed as [23]:

$$q_{beam} = \frac{3BUI}{\pi \omega^2}\left(-\frac{x_0^2 + y_0^2}{r^2}\right) \tag{6}$$

where I is the electron beam current, U is the accelerating voltage and B is energy absorption. A value of $B = 0.7$ was used in the model, as suggested in [29]. ω is the radius of the Gaussian beam and r is the radial distance from the centre of the beam spot to the point of interest on

the top surface. A value of $\omega = 100$ μm was used in the model to reflect the actual beam size used. EBM process involves melting and solidification, hence latent heat needs to be considered for the phase transformation from liquid to solid. Thermophysical properties that include material density ρ, specific heat capacity c, enthalpy H and thermal conductivity κ are all temperature dependent. These temperature-dependent properties were calculated by using the software Pandat and are presented in Table 3.

4. Results

4.1. Characterisation of PREP Ti-45Al-8Nb powders

Table 4 shows the chemical composition for main elements (in at.%) as well as interstitials (in ppm) in PREP Ti-45Al-8Nb powders. Ti, Al and Nb contents were measured to be 46.98%, 45.10% and 7.92%, respectively. Interstitial elements N and O were measured to be 130 ppm and 690 ppm. Such a low content for interstitial elements seems to be consistent with previous work on Ti-48Al-2Cr-2Nb powders with N and O contents being 30 ppm and 800 ppm in [16] and 40 ppm and 700 ppm in [14].

SEM images of PREP Ti-45Al-8Nb powders are shown in Fig. 4(a) to (c). Powder particles had a spherical shape predominantly and very little satellite particles were found in PREP powders, Fig. 4(a). The powder size distribution is shown in Fig. 4(d), where a typical bimodal characteristic can be seen. XRD spectra obtained from different powder size ranges indicate that the main phase in PREP Ti-45Al-8Nb powders was α_2-phase together with small amounts of γ-phase and β_0-phase dependent on the particle size, Fig. 5. The large sized powders (135 μm to 180 μm) has a characteristic diffraction peak representing γ-phase, whereas the presence of diffraction peak representing β_0-phase (residual β-phase from high temperature) can be seen for smaller sized particles (50 μm to 100 μm), Fig. 5. Fig. 4(b) and (c) illustrate the typical microstructure of the powders by examining their cross-sections. The dendritic structure was found to be more noticeable in the large sized powder particles, Fig. 4(b), whereas the smaller sized powder particles exhibited a smooth and featureless structure, Fig. 4 (c). The powder size dependent phase constitution in PREP high Nb-TiAl was attributed to the different solidification path and cooling rate of molten droplets in PREP process [32].

4.2. Density and Al loss in as-EBM samples

The material density of as-EBM samples was measured to be in a range from 4.17 to 4.25 g/cm^3, equivalent to the relative density of 97% to 99% with respect to the fully dense solid Ti-45Al-8Nb with the density of 4.30 g/cm^3. The measured density for groups B and C are given in Table 2. In terms of group A, the material density was measured to be 4.25, 4.23 and 4.22 g/cm^3 for samples A1, A2 and A3, respectively. There were no visible pores under the SEM examination for those samples when their relative densities (material densities) were above 99% (4.21 g/cm^3). For illustration purpose, Fig. 6 shows a SEM micrograph obtained in sample B4 where the measured density was 4.18 g/cm^3. The presence of small pores can be seen in this sample.

Table 4
Chemical composition measurement of both the PREP Ti-45Al-8Nb powders and as-EBM samples. Note: Inductively coupled plasma atomic emission spectroscopy was used to measure the chemical composition for both powders and bulk samples.

|	Element				
	Ti, at.%	Al, at.%	Nb, at.%	N, ppm	O, ppm
Ti-45Al-8Nb powder	46.98	45.10	7.92	130	690
As-EBM sample A1	48.75	43.12	8.13	140	810
As-EBM sample A2	–	43.51	–	–	–
As-EBM sample A3	–	43.62	–	–	–
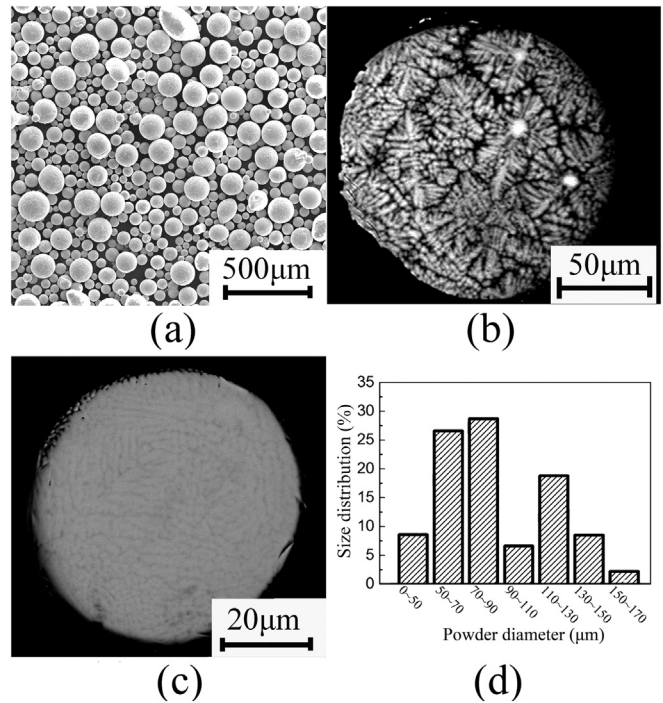
Fig. 4. (a) SEM micrograph of PREP Ti-45Al-8Nb powders; (b) BSE image of a large sized powder particle showing a dendrite structure; (c) BSE image of a small sized powder particle showing; (d) the powder size distribution.

The Al content in the as-EBM samples A1 ($I_{preheat} = 26$ mA) to A3 ($I_{preheat} = 24$ mA) were measured to be 43.12, 43.51 and 43.62 at.%, Table 4, indicating an Al loss of 1.98 to 1.48 at.% compared to the Al content 45.10 at.% in the PREP powders. In addition, the O content in the as-EBM sample was measured to be 810 ppm, Table 4, indicating an insignificant O pick-up during the EBM process compared to the O content of 690 ppm in the original PREP powders. Almost no change in N content can be found after the EBM process, Table 4.

4.3. Phase constitution and microstructure

Fig. 7 shows the normalised XRD spectra for samples A1 ($I_{preheat} = 26$ mA), A2 ($I_{preheat} = 25$ mA) and A3 ($I_{preheat} = 24$ mA), Table 1. The diffraction peak intensities in the raw XRD spectrum was normalised with respect to the maximum peak intensity, i.e. (101) plane of γ-phase. This
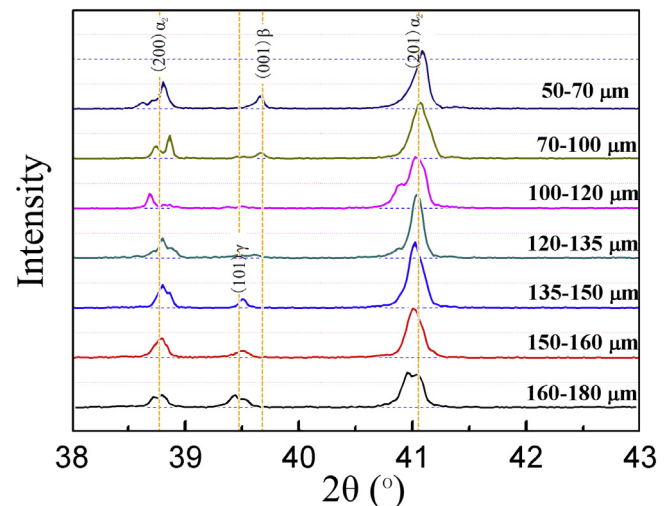

Fig. 5. XRD spectra obtained from PREP high Nb-TiAl powders with different size ranges.
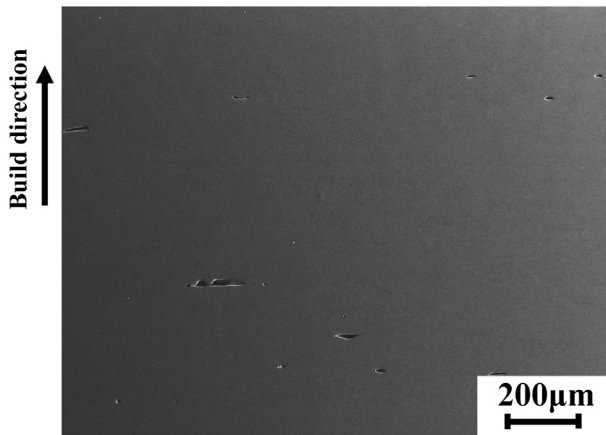
Fig. 6. SEM micrograph of sample B4 showing the presence of small pores in as-EBM condition. The sample was cross-sectioned vertically.

normalisation method was applied to all three samples. In the as-EBM samples, the phase constitution was found to be γ-phase primarily together with a small amount of α_2-phase, Fig. 7. By comparing the normalised peak intensities across samples A1, A2 and A3, it can be seen that the α_2-phase fraction decreased with the decreasing preheating beam current from 26 mA (sample A1) to 24 mA (sample A3). Unlike the PREP powders, the characteristic diffraction peak of β_0-phase cannot be seen clearly in the as-EBM sample, Fig. 7.

Fig. 8(a) to (c) shows the microstructures for samples A1 to A3. Sample A3 ($I_{preheat} = 24$ mA) had a near gamma microstructure, as revealed by the presence of equiaxed γ grains with an average size of 4.2 ± 0.2 μm, Fig. 8(c). In contrast, sample A1 ($I_{preheat} = 26$ mA) had a nearly fully lamellar γ/α_2 microstructure with an average lamellar colony size of 8.6 ± 1.7 μm, Fig. 8(a). Sample A2 ($I_{preheat} = 25$ mA) exhibited a duplex microstructure that consisted of both lamellar colony grains and equiaxed γ grains located at colony boundaries, Fig. 8(b). The average size of the lamellar colony grains for sample A2 was measured to be 11.2 ± 2.2 μm. The quantitatively measured lamellar colony grain percentage for samples A1, A2 and A3 are given in Fig. 8(d) where an increasing percentage in the lamellar colony grains can be found for the EBM samples that were fabricated with the higher preheating beam current; 82% for sample A1 ($I_{preheat} = 26$ mA), whereas 20% for sample A3 ($I_{preheat} = 24$ mA). The SEM observation that is consistent with the XRD measurement provides further evidence that the microstructure
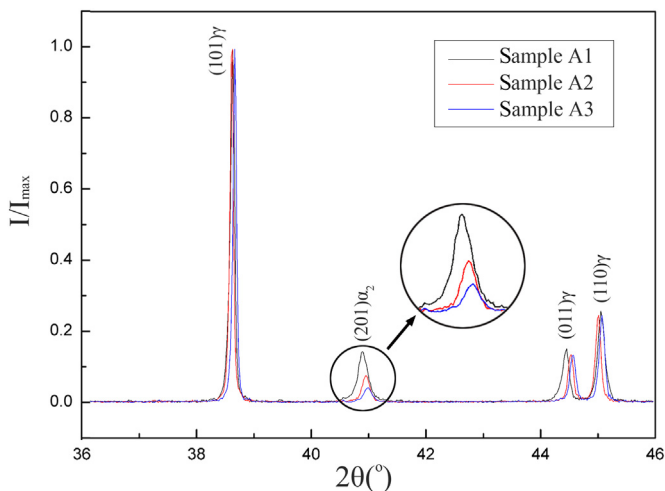
formation in EBM Ti-45Al-8Nb is strongly dependent on the preheating beam current.

Fig. 9(a) shows the TEM bright field image of a lamellar colony grain for sample A1. It is interesting to note that an α_2 lamella within the γ_3 grain in Fig. 9(a) is disintegrated, indicating the presence of microstructural degradation in the as-EBM sample. In addition, the γ lamellae with different γ variants (γ_1 to γ_3 grains) together with fine α_2 lamellae can be found in Fig. 9(a). The width of γ lamellae varied from 20 nm to 1 μm based on TEM observation. The average size of γ lamella width was measured to be 500 nm, which is similar to that of cast-TiAl [16,33]. Fig. 9(b) shows an enlarged γ grain that tended to grow at the expense of α_2 lamella located at the lower end of the TEM image. This provides another evidence of the microstructural degradation in the as-EBM Ti-45Al-8Nb sample. Few dislocations can be observed in γ grains, Fig. 9 (b). All these microstructure characteristics could be due to long-term annealing effect during the EBM process.

Fig. 10 illustrates the effect of melting parameters on the microstructure formation in EBM Ti-45Al-8Nb. As shown in Table 2, samples B1 to B4 were fabricated with different scanning speed values, whereas samples C1 to C3 were fabricated with different beam current values. In general, a duplex microstructure was found in both sample groups B and C, because the percentages of lamellar colony grains were below 60%, Fig. 10. It is evident that a higher scanning speed led to a decreased percentage of lamellar colony grains, sample group B in Fig. 10, whereas a larger beam current led to an increased percentage of lamellar colony grains. The SEM image presented in Fig. 11(a) was obtained from sample B3 that had been fabricated with a relatively low area energy of $E_A = 1.68$ W/(mm²/s), Table 2. This is a typical example for the duplex microstructure observed in sample groups B and C.

When plotting the lamellar colony grain percentage against the area energy E_A (refer to Eq. (1)) for all EBM samples, it is clear that the percentage of lamellar colony grains and E_A follows a linear relationship, Fig. 11(b). This does not necessarily mean that a higher value E_A would be always preferred for EBM Ti-45Al-8Nb. This is because an excessive energy input during the melting stage could potentially create microstructure inhomogeneity in terms of Al loss, as shown in Fig. 11 (c). In this case, sample C3 that had been fabricated with the highest area energy $E_A = 2.09$ W/(mm²/s), Table 2, is used as an example. Also shown in Fig. 11(b) is the linear relationship between the preheating area energy input and the lamellar colony grain percentage for sample group A, Table 1. When comparing the slopes of the fitted lines for both the preheating and melting stages, Fig. 11(b), it is evident that the lamellar microstructure in EBM Ti-45Al-8Nb can be more easily achieved by using a stronger preheating beam current. The underlying reason for this will be discussed together with the modelling results.

4.4. Tensile properties

Fig. 12 summarises the tensile properties at both room temperature, 800 °C and 900 °C for as-EBM samples A1, A2 and A3. All of the as-EBM Ti-45Al-8Nb samples were brittle fractured prior to yielding at room temperature; this was also the case for cast-TiAl sample. Hence fracture stress was derived from the original stress-strain curves for room temperature tests. As shown in Fig. 12, the fracture stress was measured to be 710 MPa, 715 MPa, and 670 MPa for sample A1, A2 and A3, respectively. Compared to the cast-TiAl sample with the fully lamellar microstructure (heat treated condition[3]) having a fracture stress of 580 MPa, all three EBM Ti-45Al-8Nb samples exhibited higher tensile fracture stress at room temperature. The higher tensile fracture stress in these samples could be attributed to the fine microstructure created by EBM, in particular the small sized lamellar colony grains as shown in Fig. 8. Fig. 13(a) shows the fracture surface of sample A2 at room temperature. The presence of transgranular type with river patterns can be

Fig. 7. XRD spectra for sample A1, A2 and A3 with different energy input in the preheating stage.

---

[3] Full lamellar heat treatment consists of annealing at 1340 °C followed by the furnace cooling.
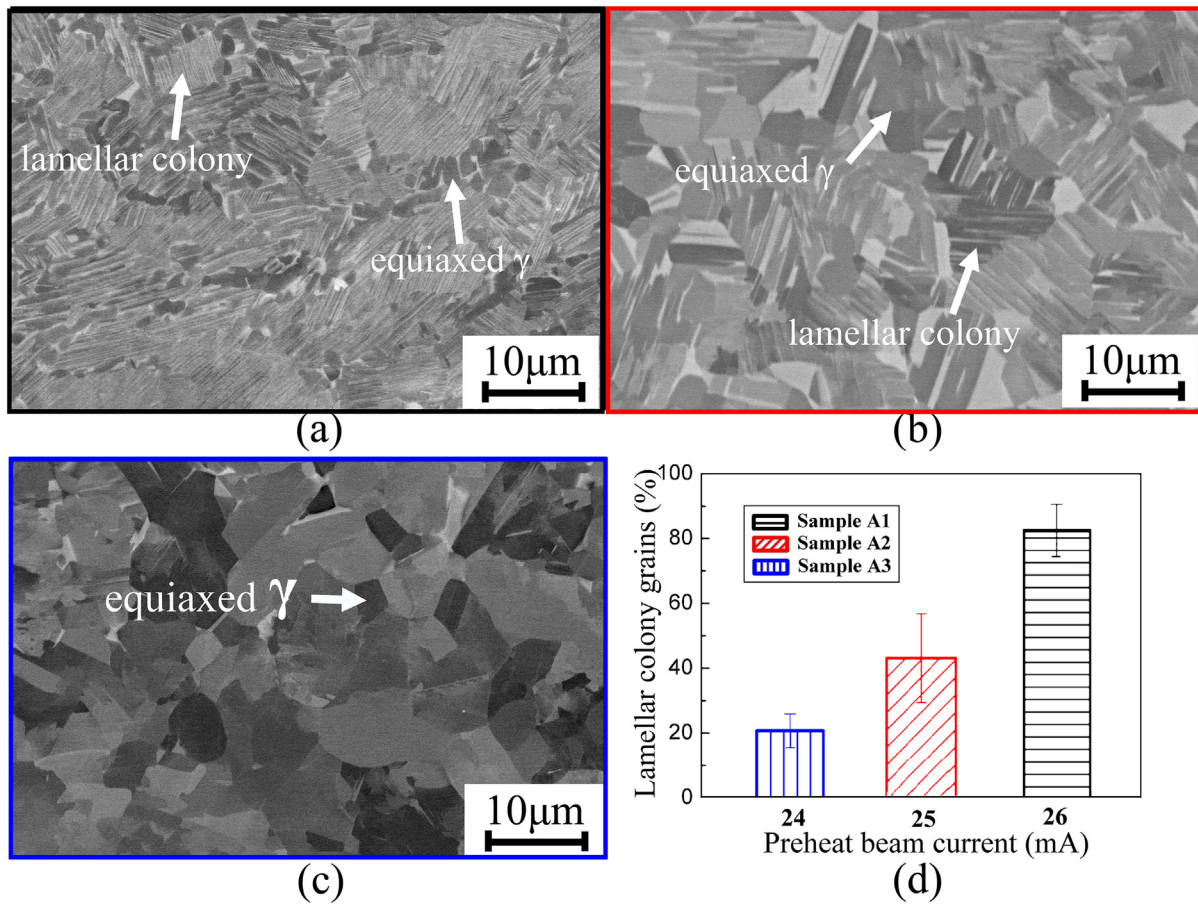
Fig. 8. Typical microstructures in EBM Ti-45Al-8Nb observed by SEM showing: (a) nearly fully lamellar microstructure in sample A1; (b) duplex microstructure in sample A2; (c) near gamma microstructure in sample A3; (d) the percentage of lamellar colony grains as a function of preheating beam current applied to samples A1, A2 and A3.

seen in sample A2, indicating a limited material ductility at room temperature.

At 800 °C, as-EBM samples A1 (820 MPa), A2 (760 MPa) and A3 (745 MPa) still exhibited much higher tensile properties compared to cast-TiAl alloy (640 MPa), Fig. 12. In this case, ultimate tensile strength (UTS) is used to make the comparison as stress-strain curves at 800 °C showed noticeable material yielding phenomenon. Accordingly, the fracture mode changed from predominantly transgranular type at room temperature, Fig. 13(a), to a mixed mode of transgranular and ductile dimples at 800 °C, Fig. 13(b). Furthermore, at 900 °C (above the DBTT temperature), the tensile strength UTS of the three EBM Ti-45Al-8Nb samples A1, A2 and A3 dropped significantly compared to those observed at 800 °C, Fig. 12. The UTS for samples A1, A2 and A3 were found to be 525 MPa, 513 MPa and 467 MPa, respectively. Apart from sample A3, EBM Ti-45Al-8Nb samples still exhibited acceptable UTS at 900 °C, when compared to the cast-TiAl (480 MPa), Fig. 12. Not surprisingly, the fracture mode at 900 °C was dominated by the ductile dimples, Fig. 13(c).
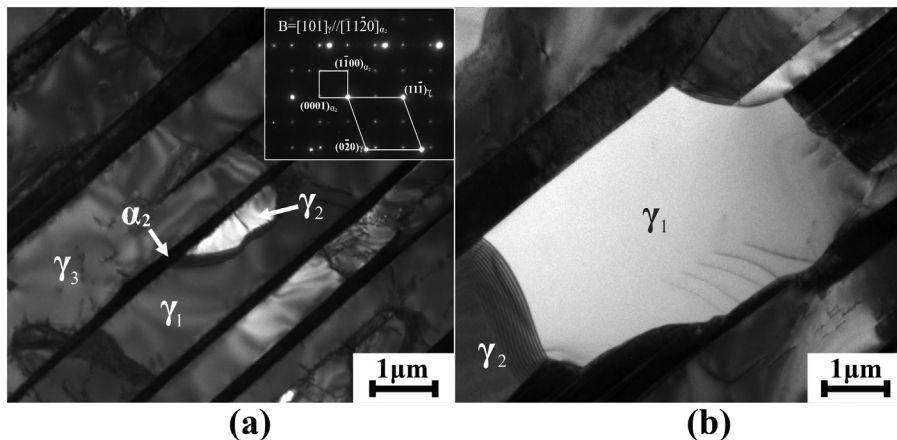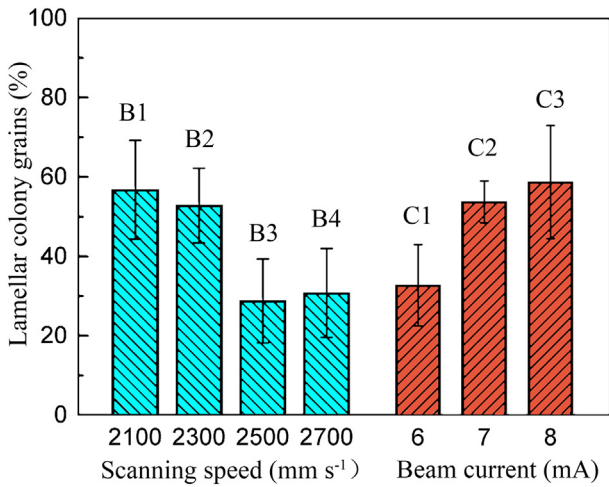

Fig. 9. TEM bright field image of a lamellar colony grain in sample A1 showing (a): α_2 lamellae within the γ grains with different variants; (b): an enlarged γ grain that tended to grow.
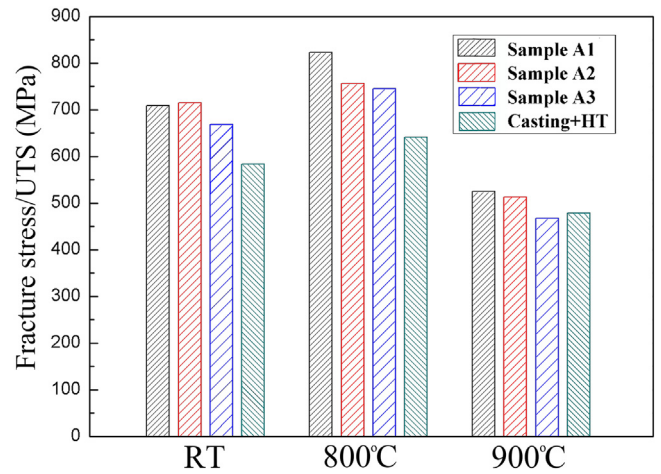
Fig. 10. The percentages of lamellar colony grains analysed based on SEM micrographs for sample groups B and C.

Fig. 12. The fracture stress/UTS measured for the as-EBM samples A1, A2 and A3, compared to the cast-TiAl sample that had been subjected to a fully lamellar heat treatment.

5. Discussion

5.1. Effect of preheating beam current on lamellar microstructure formation

As illustrated in Figs. 11(b) and 8(d), a stronger preheating beam current, $I_{preheat} = 26$ mA (or a preheating area energy input of 0.78 W/(mm²/s)) promoted the formation of nearly fully lamellar microstructure in Ti-45Al-8Nb in as-EBM condition. In comparison, the melting parameters had a less significant effect on the lamellar microstructure formation, Fig. 11(b). It is likely that a combination of higher melting beam current (>8 mA) and lower melting scanning speed (<2100 mm/s) could potentially result in a much higher percentage of lamellar colony grains compared to those as shown in Fig. 10 and Table 2. However, the measured Al loss in as-EBM sample was already ~2 at.% compared to the PREP powders, Table 4. It was reported in [7] that Al loss between 0.5 and 1.0 at.% can be achieved in EBM Ti-48Al-
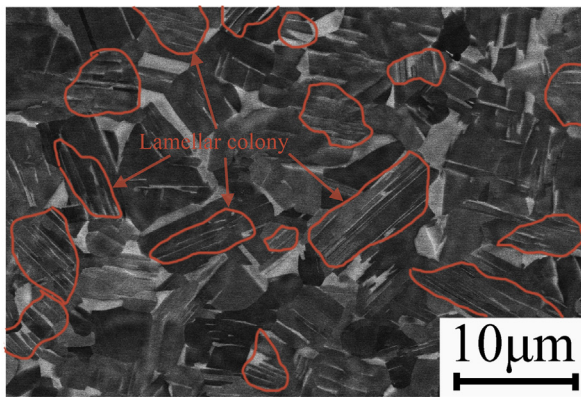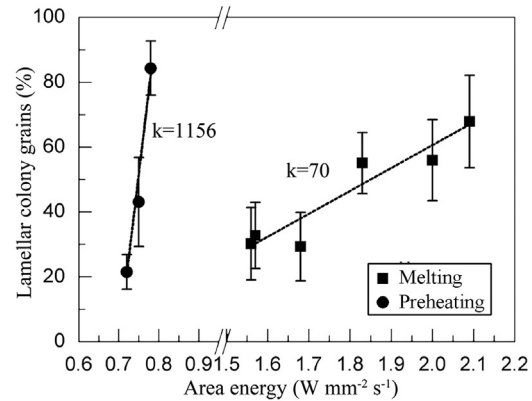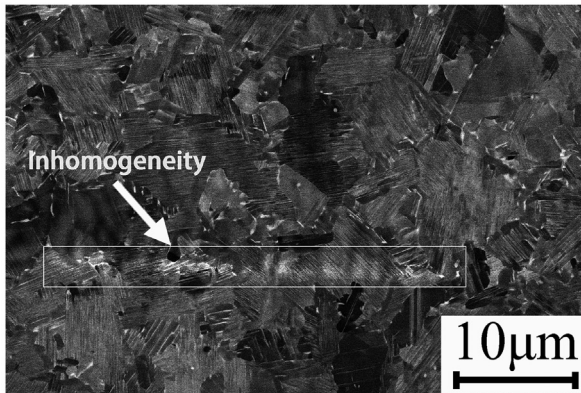

Fig. 11. (a) a duplex microstructure obtained by a low melting area energy (sample B3); (b) the percentages of the lamellar colony grains in EBM Ti-45Al08Nb samples presented as a function of area energy inputs for both the preheating and melting stages; (c) BSE micrograph for sample C3 that exhibited a nearly fully lamellar microstructure shows the presence of inhomogeneity due to Al loss.
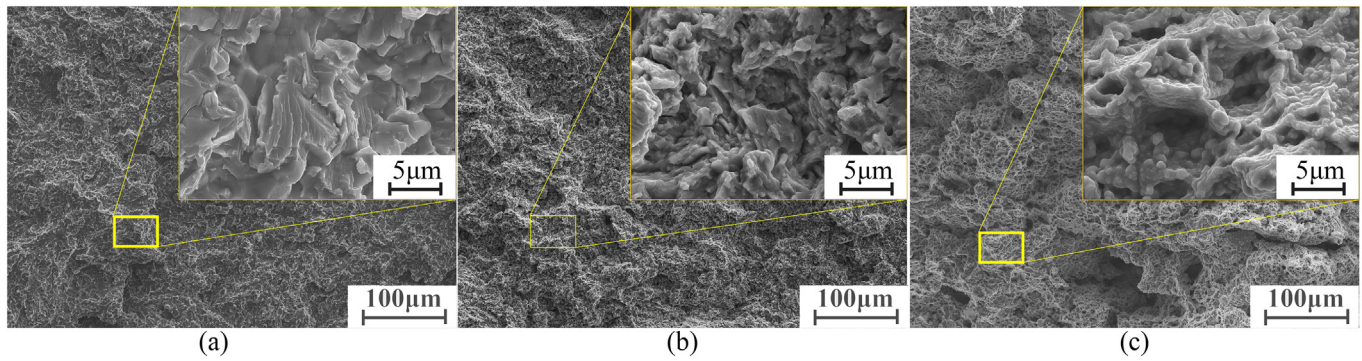
Fig. 13. SEM fractography examination of the tensile tested sample A2: (a) room temperature; (b) 800 °C and (c) 900 °C. Inset for each figure provides a higher magnification SEM micrograph.

2Nb-2Cr. Therefore, using an even stronger melting parameter sets for EBM fabricating Ti-45Al-8Nb alloy is not recommended. The build temperature was kept between 1050 and 1000 °C for EBM Ti-45Al-8Nb,[4] while the build temperature for EBM Ti-48Al-2Nb-2Cr was reported to be between 950 and 930 °C [14]. The higher build temperature could be responsible for the higher Al loss obtained in the present EBM high Nb-TiAl alloy.

Before exploring the underlying reasons for the beneficial role of using stronger preheating beam current to obtain nearly lamellar microstructure in EBM Ti-45Al-8Nb, it is important to clarify the two different terms used in EBM fabrication; build temperature and preheat temperature. The term build temperature has been used ambiguously in EBM to describe the temperature where a bulk sample was fabricated. However, in the aspect of the actual EBM processing, this temperature can only be read by a thermocouple attached to the bottom of the build starting plate. This leads to the fact that the so-called build temperature cannot reflect the real temperature, at least not accurate enough, at which the EBM sample was built. This is particularly the case for the titanium alloys (e.g. TiAl alloy and Ti-6Al-4V) that have a relatively low thermal conductivity. In contrast, the term preheat temperature, defined as the temperature prior to the EBM melting stage, is more appropriate to be used to reflect the average temperature of the top surface, as indicated in Fig. 2(a). Accordingly, changing the preheating beam current could potentially lead to a different preheat temperature. Nevertheless, it is admitted that preheat temperature cannot be easily measured experimentally. To this end, the numerical model as described in Section 3 was developed and then used here to provide temperature field for the EBM process.

Fig. 14(a) shows the temperature evolution in the preheating stage where three different magnitudes of the preheating beam current were applied. The temperature at the top surface gradually increased during the preheating stage and stabilised after 20 s, Fig. 14(a). The temperature stabilisation was due to the balance between the heat input of the electron beam and the heat loss which included heat conduction, convection and radiation as shown in Eqs. (3) to (5). The average temperature at the top surface at the finish of the preheating stage, defined as the temperature T_{local}, increased with increasing preheating beam current, Fig. 14(a). For the applied $I_{preheat}$ = 24, 25, 26 mA, temperature values of 1211, 1226 and 1241 °C were obtained from the simulation results. Fig. 12(b) presents the temperature evolution during the melting stage for three different magnitudes of $I_{preheat}$ (24, 25, 26 mA) and I_{melt} (6, 7, 8 mA). As shown in the inset of Fig. 14(b), the temperature rise was affected primarily by the applied increase in $I_{preheat}$, compared to the increase in I_{melt}. If we take the temperatures observed at the time

of 0.05 s as an example, a 1 mA increase in $I_{preheat}$ from 24 mA to 25 mA led to a temperature rise of 10 °C, whereas, a 1 mA increase in I_{melt} from 7 mA to 8 mA only led to a temperature rise of 1 °C.

It is well-known that lamellar microstructure formation in cast-TiAl alloys are very sensitive to the applied heat treatment procedure [17,34], in particular the hold time within the single α-phase temperature for annealing. To aid understanding this important point related to the EBM high Nb-TiAl alloy, the equilibrium binary phase diagram is given in Fig. 14(c) with the single α-phase region highlighted in correspondence to the modelling results in terms of the hold time within this temperature region, Fig. 14(b). After calculating the hold time and the derived percentage of hold time within the single α-phase temperature region for each parameter combination as illustrated in Fig. 14(b), it can be seen in Fig. 14(d) that the percentage of hold time within the single α-phase region was 31.9% for $I_{preheat}$ = 24 mA and I_{melt} = 7 mA (sample A3), whereas 70.8% was obtained for $I_{preheat}$ = 26 mA and I_{melt} = 7 mA (sample A1). Based on the modelling simulation results, the reason for the strong dependency of lamellar microstructure formation on the preheating beam current as shown in Figs. 8(d) and 11 can be justified. In addition, the selected preheating parameters (24 mA, 25 mA and 26 mA) not only affect the kinetics of the solidification, but also the thermodynamic equilibrium phase transformation. Due to less Al loss found in sample A3 (43.62 at.%) with $I_{preheat}$ = 24 mA compared to samples A1 (43.12 at.%) and A2 (43.51 at.%), the α-phase transition temperature can be increased according to Fig. 14(c). As a result, the hold time within single α-phase region will be reduced, according to Fig. 3, which leads to a lower percentage of lamellar colony microstructure.

In sum, the lamellar formation mechanism in EBM Ti-45Al-8Nb can be described as follow: in the case of using high preheating beam current (sample A1), the hold time for the temperature passing through single α-phase region is prolonged, hence resulting in complete phase transformation and growth of α-phase grains. These α-phase grains then transformed to lamellar colonies with γ/α2 microstructure during the cooling stage of molten pool.

To further substantiate our interpretation above-mentioned, the preheating beam current of $I_{preheat}$ = 28 mA, which is even higher than those used in Tables 1 and 2, was applied to EBM fabricate Ti-45Al-8Nb. It was first noticed that the combination of $I_{preheat}$ = 28 mA and I_{melt} = 7 mA led to the presence of severe composition inhomogeneity in the as-EBM microstructure. As a result, the value of I_{melt} was decreased to 5 mA. This parameter set leads to the creation of a Ti-45Al-8Nb sample that had a fine and fully lamellar microstructure without the presence of composition inhomogeneity, Fig. 15(a). The Al loss in this sample was measured to be 0.71 at.%. The average colony grain size was measured to be 52.7 ± 10.4 μm, Fig. 15(b). It is important to note that the width of γ-phase lamellae was relatively large, due to the use of such a high preheating beam current. This could potentially deteriorate the mechanical properties of EBM Ti-45Al-8Nb.

[4] The melting point of Ti-45Al-8Nb is approx. 1650 °C, that is at least 100 °C higher than Ti-48Al-2Nb-2Cr.
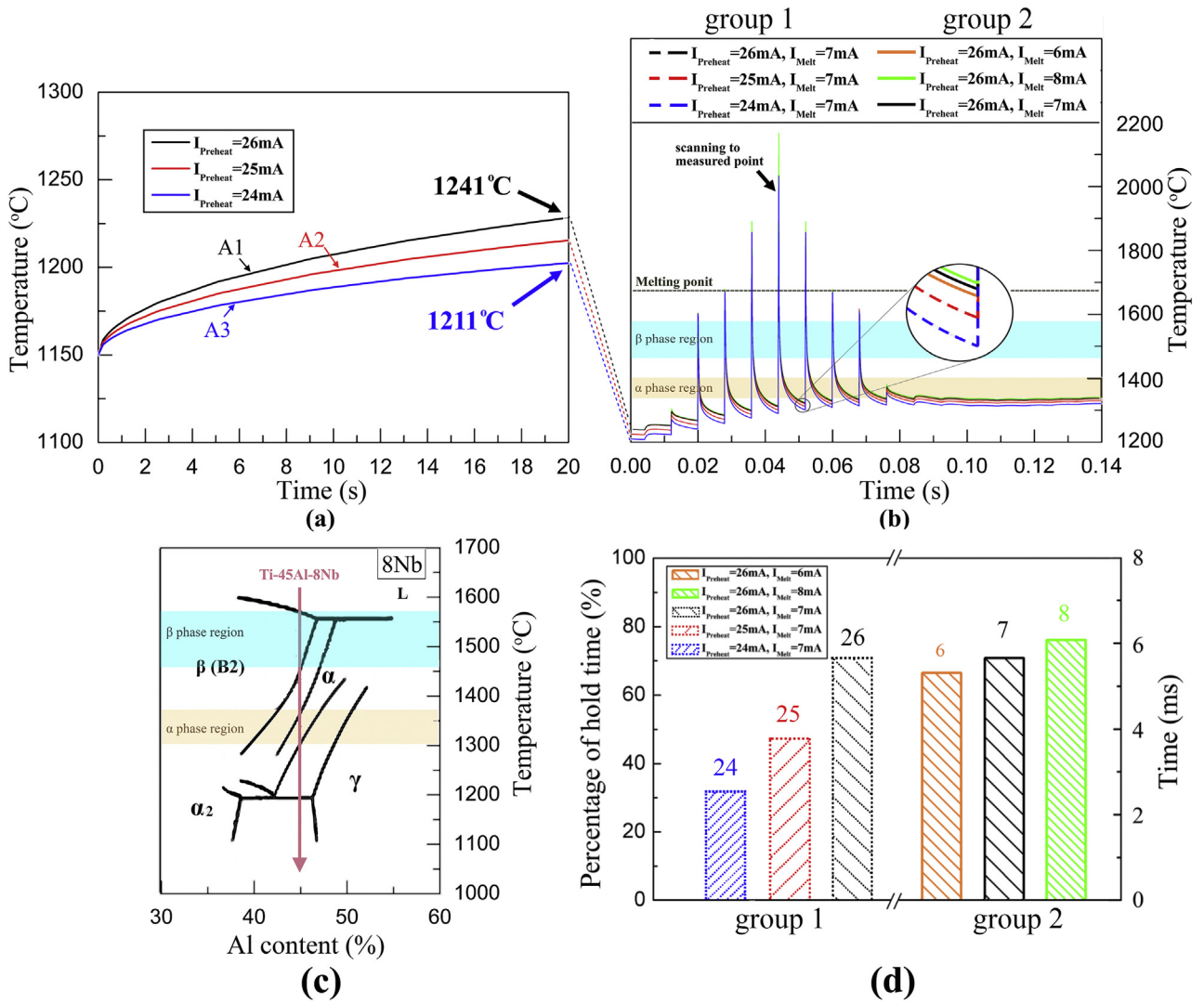
Fig. 14. (a) the temperature evolution in the preheating stage for different preheating beam currents; (b) the temperature evolution of a fixed point at the surface of sample during the melting process for different combinations of preheating and melting beam current; (c) equilibrium binary phase diagram for a Ti-Al system with 8 at.% Nb; (d) the percentage of hold time at single α-phase zone for different samples considered in (b). Note: To aid understanding the comparison between parameters, we present samples in (b) and (d) in two sample groups where group 1 is used to show the effect of melting current and group 2 is used to show the effect of pre-heat current.

5.2. Microstructure and mechanical properties in as-EBM Ti-45Al-8Nb

The absence of diffraction peak at 39.5° in Fig. 7 indicates that ordered β_0-phase in the as-EBM sample was extremely low. This is consistent with the SEM observation in Fig. 8. The absence of β_0-phase suggests that the high-temperature β-phase was completely transformed to α-phase in the as-EBM Ti-45Al-8Nb sample. The equilibrium phase diagram presented in Fig. 14(c) illustrates the typical
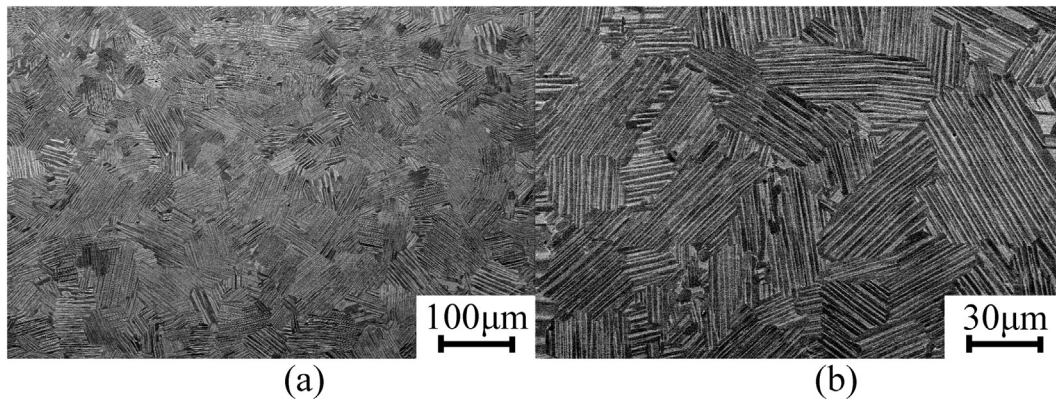
Fig. 15. SEM micrographs: (a) The fully lamellar microstructure of as-EBM Ti-45Al-8Nb alloy was obtained by using a $I_{preheat}$ of 28 mA; (b) enlarged view showing the detailed feature of lamellar microstructure on the same sample.

temperature range for β-phase being between 1450 and 1560 °C. The complete phase transformation of $\beta \rightarrow \alpha$ observed in the as-EBM sample could be due to the high preheat temperature. In addition, the cooling rate decreased less rapidly when the temperature was lower than 1400 °C, Fig. 3. For example, the cooling rate between 1650 and 1400 °C was measured to be 9.4×10^5 °C/s, whereas the cooling rate between 1380 and 1300 °C (i.e. single α-phase region) was measured to be 1.2×10^4 °C/s. Thus the cooling rate differed by almost two orders of magnitude. This indicates that a longer time duration was given to the material to achieve the complete $\beta \rightarrow \alpha$ phase transformation. Furthermore, the degree of Nb micro-segregation would be very limited due to the rapid initial solidification rate in EBM process. Small PREP powder that showed less solidification segregation because of suffering higher cooling rate can be used as a circumstantial evidence [32]. This also helped to promote a complete $\beta \rightarrow \alpha$ phase transformation.

As already commented in [14,19], the microstructure refinement in a EBM high Nb-TiAl alloy was a result of both the rapid solidification process and the cyclic annealing heat treatment. As illustrated by the temperature field simulation result in Fig. 3, after the initial solidification from the melt for the point of interest, Number 6 in Fig. 3, the material was subjected to further successive thermal exposures due to the next adjacent scan passes with $L_{off} = 100$ μm, Numbers 7–10 in Fig. 3. It is clear that temperatures exceeded several times above or within the single α-phase region, before the temperature eventually dropped below this critical temperature value, for example Number 11 and 12 in Fig. 3. Therefore, the present simulation result provides evidence to support the role of cyclic annealing heat treatment on the microstructure refinement in EBM Ti-45Al-8Nb. It is also worthwhile noting that the temperature oscillation is expected to be more frequently, due to the re-melting effect of the subsequent layers.

The microstructural degradation of α_2 lamellae disintegration can be seen in Fig. 9(a) and (b). The lamellar structure of TiAl alloy was formed under a controlled but relatively high cooling rate, Fig. 3. This led to the phase constitution of the lamellar structure being far from thermodynamic equilibrium state. It is postulated that the dissolution of initially solidified α_2 lamellae could occur during the long-term in situ annealing heat treatment during the EBM process. This accounted for the microstructural features revealed under the TEM, Fig. 9(a) and (b). This unwanted in situ annealing effect of EBM process and its consequence on microstructural degradation was also noticed in other titanium alloys, Ni-base superalloys [35] and TiAl [16]. It is very likely that the microstructural degradation is inevitable because of the thermodynamic non-equilibrium of lamellar structure. The degradation of the lamellar structure caused the phase constitution of all three samples A1 to A3 towards the equilibrium condition; this is consistent with the little difference among the three XRD spectra, Fig. 7, although the SEM micrographs in Fig. 8(a) to (c) showed different microstructures. The higher proportion of α-phase in sample A1 that was fabricated using a higher $I_{preheat}$, as highlighted in Fig. 7, could be due to the increased Al loss (Table 4). The microstructural degradation in the as-EBM Ti-45Al-8Nb samples could also be responsible for the limited improvement in their tensile properties when compared to the cast-TiAl in heat treated condition, Fig. 12. Another possible reason for the limited improvement in tensile properties of EBM Ti-45Al-8Nb could be the small fraction of porosities, as shown by the relative density measurement of 97% to 99% for the as-EBM condition. All the other microstructural features that include low content of β_0-phase, very fine lamellar colony grains as well as the low O pick-up (Table 4) provide promising prospect for EBM processing high Nb-TiAl alloys.

6. Conclusions

EBM has been used to fabricate a high-Nb TiAl alloy by using PREP Ti-45Al-8Nb powders. A fully dense and nearly fully lamellar microstructure can be obtained in the as-EBM condition. A broadened processing window was achieved by using stronger preheating beam current.

Based on the modelling results, it can be understood that the hold time for the temperature passing through single α-phase region is prolonged with the higher preheating beam current. This caused a complete phase transformation and growth of α-phase grains during the EBM processing. In the as-EBM Ti-45Al-8Nb alloy, the microstructure contained very little β_0-phase as well as very fine lamellar colony grains. This helped to improve the tensile properties in as-EBM Ti-45Al-8Nb alloy compared to the cast-TiAl in heat treated condition. However, the reason for the limited enhancement in tensile properties for the present EBM Ti-45Al-8Nb could be attributed to the presence of microstructural degradation. EBM in situ annealing effect led to α_2 lamella disintegration as evidenced by the TEM observation.

Supplementary data to this article can be found online at https://doi.org/10.1016/j.matdes.2018.09.044.

CRediT authorship contribution statement

Wenbin Kan: A student working under the supervision of Junpin Lin and Hui Peng; Proposal of the research idea; fabricating electron beam melting samples with Hui Peng; performing microstructural characterisation and mechanical testing and other experimental work; data analysis and preparing all tables and figures for the manuscript, writing the manuscript. **Bo Chen:** Proposal of the research idea; supervising the Ph. D. student, Wenbin Kan and direct the overall research activities; discussing the research outcomes with the first author, and corrections of the original manuscript. **Congrui Jin:** Proposal of the simulation part of this research. **Hui Peng:** Fabricating electron beam melting samples; helping determine the research idea, and corrections of the original manuscript. **Junpin Lin:** Providing financial support to get free-access to EBM machine, SEM and mechanical testing instruments.

References

[1] G.L. Chen, J.G. Wang, Z.Q. Sun, H.Q. Ye, Intermetallics 2 (1994) 31–36.
[2] M. Terner, S. Biamino, G. Baudana, A. Penna, P. Fino, M. Pavese, D. Ugues, C. Badini, J. Mater. Eng. Perform. 24 (2015) 3982–3988.
[3] J. Xin, L. Zhang, G. Ge, J. Lin, Mater. Des. 107 (2016) 406–415.
[4] K.F. Yao, H. Inui, K. Kishida, M. Yamaguchi, Acta Metall. Mater. 43 (1995) 1075–1086.
[5] T. Tetsui, K. Shindo, S. Kaji, S. Kobayashi, M. Takeyama, Intermetallics 13 (2005) 971–978.
[6] M.T. Jovanović, B. Dimčić, I. Bobić, S. Zec, V. Maksimović, J. Mater. Process. Technol. 167 (2005) 14–21.
[7] C. Körner, Int. Mater. Rev. 61 (2016) 361–377.
[8] E. Chauvet, P. Kontis, E.A. Jägle, B. Gault, D. Raabe, C. Tassin, J.-J. Blandin, R. Dendievel, B. Vayre, S. Abed, Acta Mater. 142 (2018) 82–94.
[9] D. Hu, X. Wu, M.H. Loretto, Intermetallics 13 (2005) 914–919.
[10] D. Cormier, O.L.A. Harrysson, T. Mahale, H. West, Adv. Mater. Sci. Eng. 2007 (2008) 1–4.
[11] L.E. Murr, S.M. Gaytan, A. Ceylan, E. Martinez, J.L. Martinez, D.H. Hernandez, B.I. Machado, D.A. Ramirez, F. Medina, S. Collins, Acta Mater. 58 (2010) 1887–1894.
[12] S. Biamino, A. Penna, U. Ackelid, S. Sabbadini, O. Tassa, P. Fino, M. Pavese, P. Gennaro, C. Badini, Intermetallics 19 (2011) 776–781.
[13] M. Terner, S. Biamino, P. Epicoco, A. Penna, O. Hedin, S. Sabbadini, P. Fino, M. Pavese, U. Ackelid, P. Gennaro, Steel Res. Int. 83 (2012) 943–949.
[14] J. Schwerdtfeger, C. Körner, Intermetallics 49 (2014) 29–35.
[15] Z.C. Cordero, H.M. Meyer, P. Nandwana, R.R. Dehoff, Acta Mater. 124 (2017) 437–445.

[16] M. Todai, T. Nakano, T. Liu, H.Y. Yasuda, K. Hagihara, K. Cho, M. Ueda, M. Takeyama, Addit. Manuf. 13 (2017) 61–70.
[17] J. Ding, M. Zhang, T. Ye, Y. Liang, Y. Ren, C. Dong, J. Lin, Acta Mater. 145 (2018) 504–515.
[18] G. Chen, Y. Peng, G. Zheng, Z. Qi, M. Wang, H. Yu, C. Dong, C.T. Liu, Nat. Mater. 15 (2016) 876.
[19] H.P. Tang, G.Y. Yang, W.P. Jia, W.W. He, S.L. Lu, M. Qian, Mater. Sci. Eng. A 636 (2015) 103–107.
[20] S. Xiao, L. Xu, H. Yu, T. Jing, Y. Chen, Trans. Nonferrous Metals Soc. China 22 (2012) 2960–2964.
[21] F. Appel, R. Wagner, Mater. Sci. Eng. R. Rep. 22 (1998) 187–268.
[22] J.G. Speight, Lange's Handbook of Chemistry, McGraw-Hill, New York, 2005.
[23] D. Dai, D. Gu, Mater. Des. 55 (2014) 482–491.
[24] N. Raghavan, R. Dehoff, S. Pannala, S. Simunovic, M. Kirka, J. Turner, N. Carlson, S.S. Babu, Acta Mater. 112 (2016) 303–314.
[25] C. Körner, H. Helmer, A. Bauereiß, R.F. Singer, MATEC Web of Conferences, EDP Sciences, 2014 08001.
[26] H. Peng, Y. Shi, S. Gong, et al., Mater. Des. 159 (2018) 155–169.
[27] X. Su, Y. Yang, J. Mater. Process. Technol. 212 (2012) 2074–2079.
[28] B. Thompson, R. Hamilton, Poult. Sci. 61 (1982) 1599–1605.
[29] A. Rai, M. Markl, C. Körner, Comput. Mater. Sci. 124 (2016) 37–48.
[30] F.J. Gürtler, M. Karg, K.H. Leitz, M. Schmidt, Phys. Procedia 41 (2013) 881–886.
[31] Y. Li, D. Gu, Mater. Des. 63 (2014) 856–867.
[32] Y. Liu, X. Liang, B. Liu, W. He, J. Li, Z. Gan, Y. He, Intermetallics 55 (2014) 80–89.
[33] F. Appel, H. Clemens, F. Fischer, Prog. Mater. Sci. 81 (2016) 55–124.
[34] Y.-W. Kim, S.-L Kim, Intermetallics 53 (2014) 92–101.
[35] Y. Kok, X.P. Tan, P. Wang, M. Nai, N.H. Loh, E. Liu, S.B. Tor, Mater. Des. 139 (2018) 565–586.